Segmented crystalline scintillators: An initial investigation of high quantum efficiency detectors for megavoltage x-ray imaging

Amit Sawant,[a] Larry E. Antonuk, Youcef El-Mohri, Qihua Zhao, Yixin Li, Zhong Su, Yi Wang, Jin Yamamoto, and Hong Du
Department of Radiation Oncology, University of Michigan, Ann Arbor, Michigan 48105

Ian Cunningham
Imaging Research Laboratories, Robarts Research Institute, London, Ontario N6A 5C1, Canada

Misha Klugerman and Kanai Shah
Radiation Monitoring Devices, Watertown, Massachusetts 02472

Electronic portal imaging devices (EPIDs) based on indirect detection, active matrix flat panel imagers (AMFPIs) have become the technology of choice for geometric verification of patient localization and dose delivery in external beam radiotherapy. However, current AMFPI EPIDs, which are based on powdered-phosphor screens, make use of only ~2% of the incident radiation, thus severely limiting their imaging performance as quantified by the detective quantum efficiency (DQE) (~1%, compared to ~75% for kilovoltage AMFPIs). With the rapidly increasing adoption of image-guided techniques in virtually every aspect of radiotherapy, there exist strong incentives to develop high-DQE megavoltage x-ray imagers, capable of providing soft-tissue contrast at very low doses in megavoltage tomographic and, potentially, projection imaging. In this work we present a systematic theoretical and preliminary empirical evaluation of a promising, high-quantum-efficiency, megavoltage x-ray detector design based on a two-dimensional matrix of thick, optically isolated, crystalline scintillator elements. The detector is coupled with an indirect detection-based active matrix array, with the center-to-center spacing of the crystalline elements chosen to match the pitch of the underlying array pixels. Such a design enables the utilization of a significantly larger fraction of the incident radiation (up to 80% for a 6 MV beam), through increases in the thickness of the crystalline elements, without loss of spatial resolution due to the spread of optical photons. Radiation damage studies were performed on test samples of two candidate scintillator materials, CsI(Tl) and BGO, under conditions relevant to radiotherapy imaging. A detailed Monte Carlo-based study was performed in order to examine the signal, spatial spreading, and noise properties of the absorbed energy for several segmented detector configurations. Parameters studied included scintillator material, septal wall material, detector thickness, and the thickness of the septal walls. The results of the Monte Carlo simulations were used to estimate the upper limits of the modulation transfer function, noise power spectrum and the DQE for a select number of configurations. An exploratory, small-area prototype segmented detector was fabricated by infusing crystalline CsI(Tl) in a 2 mm thick tungsten matrix, and the signal response was measured under radiotherapy imaging conditions. Results from the radiation damage studies showed that both CsI(Tl) and BGO exhibited less than ~15% reduction in light output after 2500 cGy equivalent dose. The prototype CsI(Tl) segmented detector exhibited high uniformity, but a lower-than-expected magnitude of signal response. Finally, results from Monte Carlo studies strongly indicate that high scintillator-fill-factor configurations, incorporating high-density scintillator and septal wall materials, could achieve up to 50 times higher DQE compared to current AMFPI EPIDs. © *2005 American Association of Physicists in Medicine.* [DOI: 10.1118/1.2008407]

I. INTRODUCTION

Portal imaging is one of the primary techniques for performing geometric verification of patient localization and dose delivery in external beam radiotherapy. In recent years, the effectiveness and, consequently, the frequency of portal imaging has been greatly accelerated by the rapid clinical adoption of active matrix flat panel imager (AMFPI)-based electronic portal imaging devices (EPIDs).[1] These devices have replaced the previous gold standard, portal film, by providing significantly improved image quality, as well as all the advantages of an inherently digital, area-detection technology.[2,3] However, recent advances in radiation therapy are placing ever-greater demands on the imaging perfor-

mance of AMFPI EPIDs. For example, the trend toward increasingly conformal treatment plans requires very accurate patient positioning, and therefore high-quality portal images. Furthermore, the increasing clinical implementation of intensity-modulated radiotherapy, which requires frequent (even daily) imaging, and investigations of megavoltage computed tomography (MVCT), which requires multiple projections, necessitate that high image quality be maintained even at very low doses.

Current AMFPI technology faces significant challenges in meeting these requirements. To date, all commercially available AMFPI EPID systems are based on indirect detection of the incident radiation, using a metal plate+phosphor screen combination for the conversion of x rays into light photons. Studies have shown that the imaging performance of these systems is x-ray quantum limited.[4,5] Thus, further improvements in imaging performance can be achieved primarily through increasing the x-ray quantum efficiency (QE) of the detector used in the imager. However, imagers based on a conventional phosphor screen detector face a severe tradeoff between x-ray quantum efficiency (which *increases* with increasing screen thickness) and spatial resolution (which *decreases* with increasing screen thickness).[6] As a result of this tradeoff, current AMFPI systems detect only ~2% of the incident radiation,[1] thus significantly limiting their imaging performance, as characterized by the detective quantum efficiency (DQE). For example, the zero-frequency DQE of current AMFPI EPIDs is ~1%,[5,7] compared to ~50% to 75% for diagnostic AMFPIs.[8–11]

There have been several efforts to incorporate high-QE detectors in AMFPI[12–14] and non-AMFPI[15–22] EPIDs. These studies have indicated that, through novel designs, it is possible to increase the DQE up to at least an order of magnitude higher than current devices. Such high-performance EPIDs would be capable of providing soft tissue contrast at megavoltage energies at low doses.[13] While this contrast may not be as high as that obtained at kilovolt (kV) energies,[23] it is likely to be sufficient for the visualization of soft-tissue structures in megavoltage images.[13,24,25] The ability to delineate soft tissue could potentially reduce the need to use surrogates such as bony landmarks. This in turn would help avoid errors due to organ motion, which has been reported to be a significant effect during radiotherapy.[26] Furthermore, recent studies involving a high QE (~30%) xenon-based detector have demonstrated that MVCT images exhibiting soft tissue contrast can be obtained at doses as low as ~2 cGy–values comparable to those used for diagnostic (i.e., kV) CT.[25]

Among the various strategies that are being explored to improve the QE of portal imagers, one of the more promising in the context of AMFPI-based EPIDs, is the development of two-dimensional (2D) matrices of thick, optically isolated converter elements made of scintillating phosphors or scintillating crystals. In a previous study, we have examined the use of segmented phosphors for megavoltage imaging.[27] In the case of segmented crystalline scintillators, preliminary investigations of CsI(Tl)-based 2D matrices for megavoltage
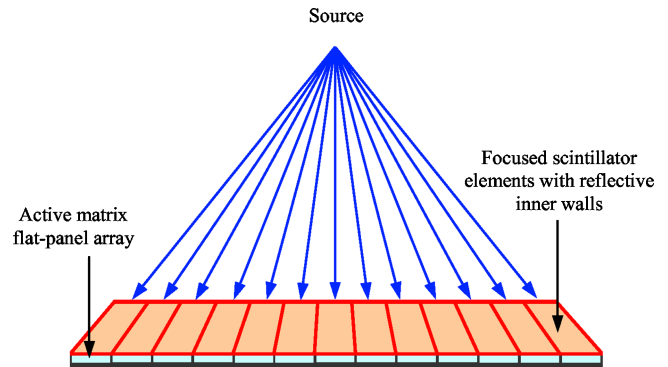

FIG. 1. Schematic cross-sectional view of an idealized indirect detection megavoltage AMFPI incorporating a focused segmented detector coupled to an active matrix flat-panel array.

x-ray imaging have been reported by Mosleh-Shirazi *et al.* using a TV-camera-based EPID[18,28] and, more recently, by Seppi *et al.* using an AMFPI EPID.[13]

In this paper, we present a systematic investigation of the feasibility and the inherent imaging performance of segmented crystalline scintillator-based detectors for megavoltage imaging. Various design considerations in the development of such detectors are examined. Radiation damage studies under radiotherapy conditions on test samples of two candidate scintillator materials, [CsI(Tl), 4.51 g/cm^3] and $Bi_4Ge_3O_{12}$ (BGO, 7.13 g/cm^3), are presented. These are followed by the results of a Monte Carlo-based study of the signal, spatial spreading and noise properties of the absorbed energy for various segmented detector configurations. These studies have been performed with respect to various design parameters such as scintillator material and height, and the thickness and material of the septa used for optical isolation. The results from the Monte Carlo studies are used to estimate the upper limits of DQE performance. Note that, in order to obtain a complete performance characterization for a segmented detector, it is also necessary to perform detailed modeling of the optical transport within the scintillator elements. However, such optical modeling is beyond the scope of the present study. Finally, we present preliminary empirical results on the signal response under radiotherapy conditions for an exploratory prototype detector, which consists of crystalline CsI(Tl) infused in a 2 mm thick tungsten matrix.

II. TECHNICAL BACKGROUND

A. Segmented scintillator concept

The use of a 2D matrix of optically isolated scintillator elements helps to circumvent the tradeoff between detector thickness (and therefore QE) and spatial resolution for an indirect detection-based x-ray converter. Figure 1 shows a schematic cross-sectional view of an idealized segmented detector coupled to an indirect detection-based active matrix array. The detector consists of optically isolated crystalline scintillator elements that are dimensionally matched (i.e., the center-to-center spacing of the scintillator elements equals the pixel pitch of the array), and registered to the pixels of

the underlying active matrix array. [A related approach involves the growth of needle-like structures of CsI(Tl), which serve as light guides, on the active matrix array. However, the CsI(Tl) needles exhibit significant optical crosstalk, which increases with detector thickness.[29,30] Consequently, the tallest reported structures used for therapy imaging are ~0.8 mm,[24] and are capable of yielding only marginal improvement in QE.] For thicker segmented detectors, on the order of 10 mm or more, the elements should, ideally, be "focused" toward the x-ray source so as to avoid spatial resolution at field boundaries due to off-axis x rays—an effect that may become increasingly important for large-area fields. Under ideal conditions of registration and optical coupling between the detector and the active matrix array, along with complete optical isolation of the scintillator elements, the thickness (and thereby, the QE) of such a detector can be increased without loss in spatial resolution due to the spread of optical photons. Note that, in the present work, we will concentrate only on "non-focused" detectors, in order to simplify the study of the inherent imaging properties of various detector configurations.

B. Analysis techniques for performance characterization of segmented detectors

Fourier-based metrics such as the modulation transfer function (MTF) and Wiener noise power spectrum (NPS) were originally developed, and have been widely used, for the characterization of linear (or linearizable), spatially invariant, and wide-sense stationary imaging systems. Most digital-imaging technologies do not meet these requirements. However, Fourier methods can be used to describe the "presampling" MTF which correctly describes the resolution characteristics of a digital system—with the exception of aliasing issues that become increasingly important as the feature size of the object being imaged approaches that of the pixel spacing of the imager.[31–33] Fourier methods can also be used to describe the NPS of wide-sense cyclostationary processes, which require the mean and autocorrelation to be periodic.[34,35] These conditions are satisfied for digital systems in which the mean and autocovariance are invariant to shifts of an integer number of detector elements (i.e., wide-sense stationary in "discrete" space).[32]

It is interesting to note that (see the Appendix) these concepts also apply to segmented detector-based imaging systems such as those described in this paper and elsewhere,[27] even though the segmented detector has a distinctly shift-variant response. This is true as long as the segmented detector response is invariant with respect to shifts of integral multiples of the element spacing and the elements are registered to the photodiode array elements. In the absence of such registration, Fourier methods should be used with caution.[36]

C. Design considerations

The practical implementation of the segmented detector concept requires careful consideration and optimization of several design parameters such as scintillator material, detector height, and the material, and thickness of the septa used for optical isolation. These parameters impact the energy absorption and the optical transport properties of the detector, both of which are important determinants of imaging performance. However, in this study, we will examine the above-mentioned design parameters primarily with respect to their effect on the energy absorption properties, and thereby, the signal and noise transfer characteristics of a detector.

In this work, a "DQE-based" approach is adopted toward optimizing detector design. Frequency-dependent DQE is a widely accepted metric of x-ray imaging performance, and can be expressed as follows:[32,37]

$$DQE(u) = \frac{q_0 \times G^2 \times T_{sys}^2(u)}{S_{sys}(u)},\qquad(1)$$

where u represents the independent spatial frequency variable, q_0 is the total number of incident quanta per unit area, G is the system gain, $T_{sys}(u)$ and $S_{sys}(u)$ are the MTF and NPS, which characterize the spatial resolution and the noise transfer properties of the imaging system, respectively. DQE can also be expressed as the ratio of the squared output signal-to-noise ratio (SNR) to the squared input SNR.[38] It is useful to represent an imaging system as a cascade of linearly coupled stages.[39,40] In such a view, the input signal and noise are transferred through each stage via amplifying and/or scattering processes, with the output of each stage serving as input to the next stage. From this description it is clear that, in order to maximize the SNR transfer efficiency (and therefore, the DQE) of the entire imaging system, it is necessary to optimize SNR transfer within the detector. In the context of this paper, we shall refer to the squared SNR transfer efficiency of the detector up to the energy absorption stage as the *intrinsic detector DQE* (DQE_{ID}). The remainder of this section describes the various design parameters with respect to their potential impact on DQE_{ID}.

1. Scintillator: Material and thickness

In an indirect detection-based AMFPI, a scintillator serves to detect the incident radiation and generate light photons, which are detected by the underlying active matrix light-sensor array. It can be seen from Eq. (1) that, in order to maximize the DQE_{ID}, the scintillator should exhibit high gain while simultaneously minimizing the spread of absorbed energy in order to maintain adequate spatial resolution. The gain of a scintillator is the product of its x-ray quantum efficiency (QE), the average number of light photons generated per x-ray interaction, and the average probability of a light photon exiting from the array side of the scintillator.

For x-ray-quantum-limited systems such as megavoltage AMFPIs, the component of gain that serves to improve the DQE is the quantum efficiency of the detector. For a given scintillator material, the detector thickness is a direct determinant of the x-ray quantum efficiency, i.e., the QE increases with thickness. However, a thicker scintillator also provides longer paths for the lateral spread of secondary electrons and x-ray photons, resulting in a loss of spatial resolution. While

this effect is conceptually similar to the tradeoff between detector thickness and spatial resolution due to optical spread, the loss of spatial resolution due to secondary radiation becomes significant only at much higher values of detector thickness (a few centimeters for crystalline scintillators compared to a few hundred microns for powdered phosphors).[41] In order to achieve high QE while minimizing the spread of secondary radiation, it is useful to consider high-density and high-atomic number scintillators. Such materials not only detect a larger fraction of the incident radiation, but are also likely to reduce the lateral spread of secondary electrons and photons.[41]

It is also highly desirable that the scintillator exhibits adequate light output as well as good optical transmission properties in order to ensure a sufficiently high optical gain (i.e., the number of light photons detected by the active matrix array, per interacting x ray) so as to maintain x-ray-quantum-limited operation of the imaging system. Moreover, good optical transmission is also important in minimizing depth dependence of the optical gain—an effect that may cause significant reduction of the DQE due to increased optical Swank noise.[27] Finally, the scintillator should exhibit good resistance to the high doses of radiation that are encountered in radiotherapy imaging. Such high doses diminish the light output of a scintillator primarily due to the formation of "color centers."[42,43] As a result, the scintillator exhibits higher attenuation of certain wavelengths of light. In addition, very high doses also cause damage to the scintillation mechanism of the crystal, resulting in fewer light photons being generated per interacting x-ray photon.[42,43] Thus, in order to maintain x-ray-quantum-limited operation of the imager over several years of clinical use, a high degree of tolerance to radiation damage is desirable.

2. Septa: Material and thickness

The primary function of the septa is to confine light in a scintillator element so that the optical photons generated as a result of x-ray interactions within a given element reach only the underlying array pixel. Toward achieving this goal, it is desirable that the septa be opaque, in order to avoid optical cross talk between adjacent elements, and highly reflective, so that a very large fraction of the light that is generated within an element is directed toward the underlying array pixel. The septa may be fabricated from low-density materials like epoxies or polymers, or from high-density materials like copper, tungsten, or alloys. In the case of low-density septa, in addition to the requirements of opacity and reflectivity stated above, it is desirable that the septa be as thin as mechanically feasible. Thinner septa ensure higher "fillfactor" for the scintillator, which in turn results in a larger fraction of the incident x rays being detected.

The situation is somewhat more complex in the case of high-density septa. On the one hand, such structures can serve a function analogous to that of the copper build-up plate, i.e., the septa detect a fraction of the incident radiation and generate secondary electrons and photons that escape into the surrounding scintillator elements, thereby enhancing the detector QE. On the other hand, secondary electrons and photons produced within a given septal wall may be absorbed by multiple, adjacent scintillator elements, thus degrading the spatial resolution. As is the case for low-density septa, thicker high-density septa will decrease the scintillator fill factor, although some of this decrease may be compensated by the localized build-up effect described above. Similarly, the loss in resolution due to increased scatter caused by secondary electrons and photons generated within the septa may be countered by the fact that thicker, denser septal walls will be better at limiting the spread of absorbed energy within the scintillator. In the context of these competing effects, it is therefore necessary to carefully optimize the thickness and density of septa in order to achieve good detector performance.

III. METHODS

Empirical and theoretical studies were performed on two candidate scintillator materials CsI(Tl) and BGO in order to investigate the feasibility of segmented scintillator-based detectors for therapy imaging, and identify configurations that yield optimal performance. The studies consisted of radiation damage experiments, a Monte Carlo-based theoretical examination of 100 different segmented detector configurations, and measurements of signal response under radiotherapy conditions for an exploratory prototype segmented detector.

A. Radiation damage

As discussed in Sec. II C 1, scintillators used in segmented detectors should exhibit a high degree of radiation damage resistance over a dose range that is consistent with several years of operation of the imager. Both of the scintillators examined in the present study have been shown to exhibit large variations in resistance to radiation damage, depending on the manufacturer, presence of impurities, irradiation conditions, etc. For example, various studies indicate that BGO exhibits between 3.5% and 20% decrease in light output after $\sim 10^4$ Gy absorbed dose.[44–47] Similarly, the light output of CsI(Tl) has been reported to decrease between 7% to 25% after $\sim 10^4$ Gy.[43,48–52] (For both materials, the above values correspond to the highest quality samples examined in each study.) In order to characterize the radiation damage under irradiation conditions representative of those encountered in radiotherapy imaging, studies were performed on CsI(Tl) and BGO samples using a 6 MV photon beam from a radiotherapy linear accelerator. The relative change in light output was determined as a function of dose. Two sets of scintillator samples were used—an irradiated set and a control set. Each set consisted of one CsI(Tl) ($20 \times 17 \times 14$ mm^3) and one BGO ($30 \times 6 \times 6$ mm^3) crystal. For each scintillator, the samples were obtained from the same single crystal block and are therefore assumed to have identical properties.

1. Irradiation

The irradiated sample set was inserted into dimensionally matched cavities created in the center of a $20 \times 20 \times 3$ cm^3 acrylic slab. The samples were placed horizontally (i.e., with the longest dimension perpendicular to the beam direction) into the cavities and the slab was sandwiched between two other acrylic slabs—one 2.7 cm thick, placed on the near side of the x-ray source to provide buildup and another, 4.5 cm thick, placed on the far side of the source to provide backscatter. The combination of the three slabs was placed in close proximity to the treatment window of a Varian 21-EX linear accelerator (linac). In this setup, the samples were located at a source-to-detector distance (SDD) of 56.8 cm (measured from the source to the sample surface nearer to the x-ray side). The field size was adjusted to 10×10 cm^2 at the isocenter. Irradiations were performed with a 6 MV photon beam on a weekly basis for five weeks, in order to deliver a cumulative *equivalent dose* of 2500 Gy, where we define equivalent dose as the dose absorbed by water, instead of the crystal, in an identical setup placed at a SDD of 130 cm (corresponding to a typical clinical imaging distance).

2. Sensitivity measurements

The effect of radiation damage on the two crystalline materials was determined by measuring the change in the x-ray sensitivity (light output per unit incident radiation) of the irradiated samples relative to that of the control samples. Sensitivity measurements were performed on the control and the irradiated samples before and immediately after each irradiation. The samples were inserted vertically into cavities created in the center of a $25 \times 25 \times 4$ cm^3, black, foam block such that only one side of each sample was visible. The block was placed on a 512×512 pixel, 508 μm pitch, indirect detection array, Cyclops-II, previously developed for megavoltage imaging applications,[2,5] with the open side of the crystals in direct contact with the array pixels. The array was placed at a SDD of 130 cm, with a field size of 10 $\times 10$ cm^2 at the isocenter. Each measurement was obtained from the same set of array pixels, thus eliminating any discrepancies due to inter-pixel gain variations. In addition, each set of measurements on the irradiated samples was preceded by corresponding measurements on the control samples, in order to eliminate any effects of daily/weekly variations in linac output and also to compensate for any change in light output of the irradiated samples due to radiation absorbed during the course of the sensitivity measurements. Light output from the crystals was measured as a function of the number of beam pulses delivered, and the x-ray sensitivity was calculated from the slope of this response characteristic. The sensitivity value from each irradiated crystal was normalized with respect to that obtained from the corresponding control.

B. Monte Carlo studies

As discussed in Sec. II C, the imaging performance of a segmented detector is determined by a number of design parameters. The effect of parameters such as scintillator material and thickness, and septal material and thickness, was studied through Monte Carlo simulations using the EGSnrc Monte Carlo code[53] and the DOSXYZnrc user code.[54] A variety of segmented detector configurations were examined with respect to the signal, spatial resolution, and noise properties of the x-ray energy absorbed in each detector. All simulations were performed using a 6 MV photon spectrum corresponding to a Varian linac.[55] The ECUT and PCUT parameters, which determine the cut-off energies for electron and photon transport, were specified as 0.521 MeV (corresponding to a kinetic energy of 0.01 MeV) and 0.005 MeV, respectively. For each simulation, the detector was configured with an overlying 1 mm thick, Cu plate, corresponding to the build-up plate used in commercially available AMFPI EPIDs.[1] The complex geometry of the segmented detector, required as input to the DOSXYZNRC program, was created using an in-house MATLAB routine that allows the user to specify various parameters such as external dimensions of the detector, size of the scintillator elements, septal thickness, etc. Calculations were performed in order to determine the energy deposited in the scintillator elements of the segmented detector and not the septal walls. (While the septa do affect the energy deposition within the scintillator elements, they do not generate optical photons.) For all configurations, the voxel pitch was chosen to be 508 μm—equal to the pixel pitch of the Cyclops-II array.[2]

1. Signal

In the context of the Monte Carlo simulations presented in this work, signal is defined as the amount of energy (in joules) deposited per detector element. The average amount of energy deposited per detector element was estimated for 100 different detector configurations based on combinations of two scintillator materials [CsI(Tl) or BGO], high or low density septa (tungsten or polystyrene, respectively), five scintillator thicknesses (ranging from 5 to 40 mm) and five septal wall thicknesses (from 50 to 250 μm). The segmented detector was modeled as a matrix of 200×200 voxels, where each voxel consisted of a scintillator element surrounded by septal walls on four sides. Energy was deposited in the detector elements by a 10×10 cm^2, parallel, photon beam, perpendicularly incident on the *X-Y* plane of the detector. A total of 20 million photon histories were used for each detector configuration, and the average energy deposited in a scintillator element was computed from the mean of the values obtained from the central 100×100 elements. The large number of histories, along with the summing of the values in the central elements, resulted in statistical uncertainties of less than 1%.

2. Presampling modulation transfer function (MTF)

An upper limit to the spatial resolution of a segmented detector is defined by the product of the MTF corresponding to the spread of the absorbed energy and the sinc function corresponding to the dimensions of each optically isolated scintillator element. In the present work, this product shall be referred to as the presampling *intrinsic detector MTF* (MTF_{ID}), as it represents the inherent spatial resolution of a segmented detector configuration for a given input energy spectrum. The MTF_{ID} was determined for several detector configurations through a Monte Carlo calculation that emulated the angled slit technique[56]—a method widely used to determine the presampled MTF for digital imaging systems.[37] A detailed discussion on the determination and interpretation of the line spread function (LSF) and presampling MTF for a segmented detector can be found in the appendix of this paper.

The simulation geometry consisted of a 30×0.0004 cm^2 photon beam (using 90 million histories), perpendicularly incident on the *X-Y* plane of the segmented detector, at an angle of $0.3°$ with respect to one of the axes. The segmented detector consisted of 600×600 voxels, corresponding to an area of $\sim 30 \times 30$ cm^2. Simulations were performed for 10 and 40 mm thick BGO and CsI(Tl) scintillators, incorporating 50 μm thick, high-density (tungsten) and low-density (polystyrene) septal walls. In addition, in the case of the 40 mm thick CsI and BGO scintillators, simulations were also performed for configurations incorporating thicker (100 and 150 μm) tungsten walls. In each case, the line spread function (LSF) was calculated and the magnitude of the Fourier transform of the LSF yielded the MTF_{ID}.

3. Noise power spectrum (NPS)

The noise transfer properties of the various detector configurations described above were studied by estimating the noise power spectrum of the energy absorbed within the scintillator—hereafter, referred to as NPS_{ID}. The detector geometry was identical to that used to obtain the MTF_{ID}. In each case, the detector was irradiated with a 30×30 cm^2 photon beam perpendicularly incident on the *X-Y* plane of the detector. For each detector configuration, a set of 40 independent "absorbed energy frames" was obtained, using 90 million photon histories per frame in order to ensure that statistical errors per voxel were below 10%.

The one-dimensional NPS_{ID} for each detector configuration was determined using the synthesized slit technique[57] as follows. The spatial distribution of the absorbed energy recorded in the central 500×500 scintillator elements of each frame was used to form ten independent nonoverlapping blocks or slits, each forming a matrix of dimensions 250×100. Thus, each 40 frame set, corresponding to a given detector configuration, yielded 400 independent slits. The values in each slit were summed along the narrow (y) dimension to yield 400 independent, 250-point realizations. (The summing operation also served to further reduce the statistical error in the values of each of the 250 points.) A one-dimensional discrete Fourier transform (DFT) was applied to

FIG. 2. Segmented detector prototype consisting of CsI(Tl) injected into a 2 mm thick tungsten matrix of 40×40 cells of 1 mm pitch and a septal wall thickness of 50 μm (equal to that used in the theoretical calculations).

each of the 400 realizations and the 1D NPS_{ID} was estimated from the expectation value of the resulting power spectra from[32]

$$NPS_{ID} = \frac{x_0 y_0}{N_x N_y} \left\langle \left| DFT\left(\sum_{n_y=0}^{N_y-1} \Delta d_{n_x,n_y} \right) \right|^2 \right\rangle J^2 mm^2, \quad (5)$$

where x_0 and y_0 are the center-to-center spacings (in millimeters) of the scintillator elements, N_x and N_y are the number of elements in the x and y dimensions, respectively, and d_{n_x,n_y} is the energy deposited (in joules) within the (x,y)-th element and

$$\Delta d_{n_x,n_y} = d_{n_x,n_y} - \langle d_{n_x,n_y} \rangle. \quad (6)$$

4. Detective quantum efficiency

The one-dimensional, frequency-dependent, intrinsic detector DQE (DQE_{ID}) was calculated using

$$DQE_{ID} = \frac{A^2 MTF_{ID}^2}{q_0 NPS_{ID}}, \quad (7)$$

where A equals $q_0 \times G$ [see Eq. (1)] is the average energy deposited in a scintillator element. The incident photon fluence q_0 is calculated by dividing the number of photon histories by the surface area of the detector. The DQE_{ID} establishes an upper limit for the DQE performance of an imaging system configuration employing a given detector, i.e.,

$$DQE_{sys} \leq DQE_{ID}. \quad (8)$$

C. Empirical signal characterization of a prototype segmented detector

An exploratory prototype segmented detector, shown in Fig. 2, was fabricated by infusing crystalline CsI(Tl) into a $40 \times 40 \times 2$ mm^3 tungsten matrix composed of 50 μm thick septa. The infusion was performed by placing the tungsten matrix in a crucible and completely covering the matrix with CsI(Tl) powder. The temperature inside the crucible was gradually raised from room temperature to above 626 °C—the melting point of CsI(Tl melts at a lower temperature of 440 °C). The molten CsI(Tl) was allowed to

completely fill the open cells of the tungsten matrix and the temperature was gradually lowered over ~72 hours, allowing the CsI(Tl) to cool down and crystallize. Finally, the excess CsI(Tl) encasing the tungsten matrix was carefully polished away.

The resulting detector consisted of 40×40 elements, with a pitch of 1 mm. Since the voxel pitch was not an integral multiple of 508 μm—the pitch of our radiotherapy active matrix array[2] (the tungsten matrix having been originally fabricated for a different study), the signal response was studied by coupling the prototype detector to a high-resolution (127 μm pitch) indirect detection array, originally developed for diagnostic imaging applications.[58] By over-sampling the segmented detector in this manner, it was possible to obtain a signal profile for each voxel. (Owing to the insufficiently large area of the prototype detector as well as the lack of pixel matching, it was not possible to make frequency-dependent measurements such as MTF, NPS, and DQE.) The detector was coupled to the active matrix array such that the horizontal and vertical lines of the tungsten grid were parallel to the gate and data lines of the array. The measurement conditions were identical to those described in Section III A 2, with the exception that, in this case, a 1 mm thick Cu plate was used as a build-up layer. The surface of the Cu plate in contact with the CsI(Tl) was blackened in order to avoid the reflection of optical photons from the Cu plate back into the detector. Such an arrangement helped minimize optical scatter and consequent blurring of the signal response. The signal response was recorded as a function of irradiation time in monitor units (MUs) of the linac. [According to the calibration factor used for linac, 1 MU corresponds to 0.8 cGy deposited in water at a source-to-detector distance (SDD) equal to 100 cm, with 10 cm overlying water, for a field size of 10×10 cm^2 at the isocenter (i.e., 100 cm SDD)]. The x-ray sensitivity was determined from the slope of the signal response characteristic.

IV. RESULTS

A. Radiation damage

Figure 3 shows the effect of radiation-induced damage on the x-ray sensitivity of the CsI(Tl) and BGO samples. Between the two scintillator materials, CsI(Tl) exhibits slightly superior radiation damage tolerance compared to BGO. It can be seen that there is no significant difference between the post-radiation sensitivity obtained in a given week and the preradiation sensitivity obtained the following week, indicating the absence of short-term room-temperature annealing. Most importantly, both scintillator materials exhibit a relatively gradual decrease in sensitivity, with less than 15% loss after ~2500 Gy equivalent dose. From the records available at our institution, this dose corresponds to more than five years of clinical operation of an imager. Since both CsI(Tl) and BGO have sufficiently high light output (~61 000 and ~8500 photons/MeV, respectively[59]), this result indicates that a megavoltage x-ray imager incorporating these scintillators is likely to remain x-ray quantum limited over at least several years of normal clinical operation. Furthermore,
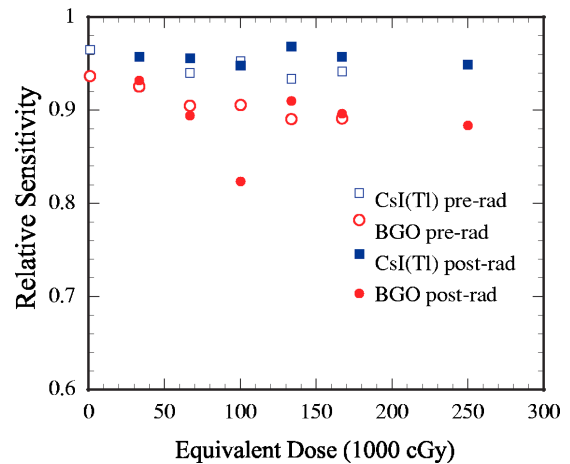

FIG. 3. Effect of radiation-induced damage to the signal-response characteristics of CsI(T1) and BGO samples in terms of measured x-ray sensitivity at 6 MV as a function of equivalent dose. The sensitivity values have been normalized with respect to those obtained from "control" samples of CsI(T1) and BGO, having identical dimensions and obtained from the same corresponding single-crystal ingot. The open and closed symbols correspond to measurements taken before and after irradiation, respectively. Therefore, the first set of data points (0 Gy) shows only open symbols while the last set (2500 Gy) shows only closed symbols. The anomalous data point corresponding to the third post-radiation measurement on BGO, lying significantly outside the general trend, is believed to be the result of a measurement error.

regular calibration procedures may be used to correct for any gradual decrease in the light output over time, as well as any spatial variations in the light output that may occur as a result of different parts of the detector receiving different amounts of cumulative dose.

B. Monte Carlo studies

1. Signal properties

Figure 4 shows the average energy absorbed within a scintillator element for 100 different configurations of segmented detectors. Results are shown as a function of septal wall thickness for CsI(Tl) and BGO detectors ranging from 5 to 40 mm in height, and incorporating low density (polystyrene) or high-density (tungsten) septal walls. A number of trends can be observed from these calculations. First, the average energy absorbed within a scintillator element increases with increasing scintillator thickness and diminishes with increasing wall thickness—the latter effect being more pronounced for taller detectors. The latter effect occurs even for configurations incorporating tungsten walls, indicating that the signal contribution due to the build-up effect of high-density septa (see Sec. II B 2) is relatively small compared to that due to energy directly absorbed within the scintillator. Second, as expected, detector configurations based on the higher density scintillator BGO exhibit ~1.5 to 2.0 times higher energy deposition per element compared to the corresponding CsI(Tl)-based configurations. Finally, and perhaps somewhat contrary to expectation, tall detectors (greater than ~30 mm) employing polystyrene septa exhibit significantly higher energy deposition per element compared to corre-
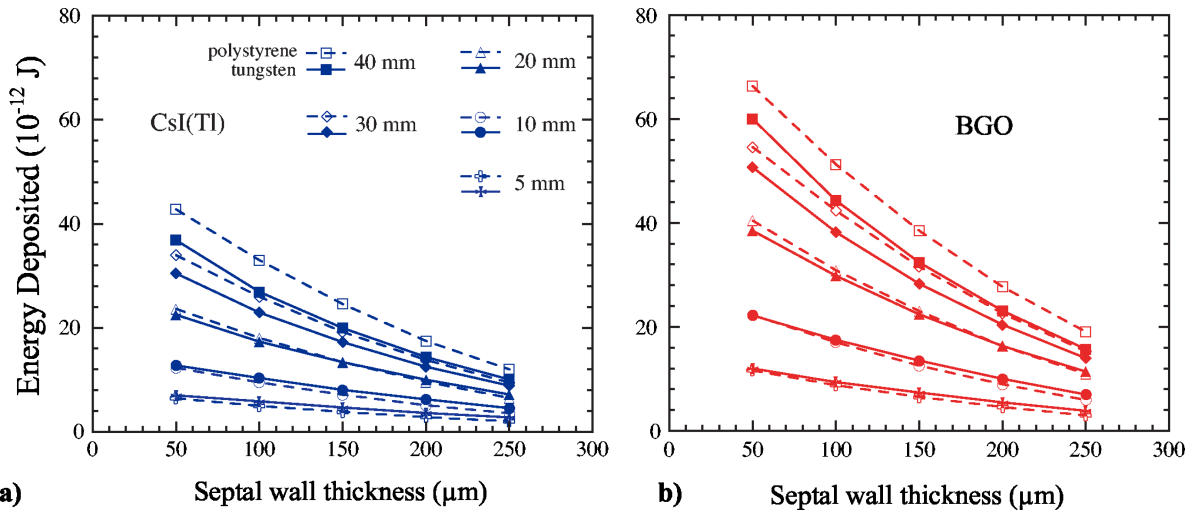
FIG. 4. Average energy deposited per scintillator element for a variety of (a) CsI(T1) and (b) BGO segmented detector configurations ranging from 5 to 40 mm in thickness. The energy deposited per element is plotted as a function of increasing septal thickness. Note that the absolute value of the energy depends on the number of histories used in the Monte Carlo simulation. In order to better illustrate trends, the data points are connected using dashed and solid lines for polystyrene and tungsten septa, respectively.

sponding configurations that use tungsten septa. This is because low-density septa are relatively ineffective in preventing "cross talk" between voxels, i.e., a scintillator element surrounded by low-density septa receives a significant fraction of the total energy deposited from secondary electrons and photons generated in adjacent cells—an effect that is strongly inhibited in configurations employing the higher-density, tungsten septa.

2. Spatial resolution

Figures 5(a) and 5(b) show the line spread functions (LSFs) obtained from Monte Carlo simulations, based on the angled-slit method, for a 40 mm thick, CsI(T1) segmented detector, incorporating polystyrene and tungsten septa, respectively. Also shown for comparison is a LSF obtained using the same method for a 40 mm thick detector with both

the scintillator as well as the septa composed of CsI(T1)—in effect, making it a homogeneous slab of CsI(T1). The LSFs for the polystyrene and tungsten-based configurations exhibit sharp dips and peaks, respectively, at regular intervals.

The appearance of these peculiar features in the LSF can be explained as follows. The angled slit method approximates the process of scanning a slit beam across a detector and recording the signal at the central detector element, for each position of the slit beam, in order to generate the LSF.[56] At positions where the slit beam is completely incident on the septal walls, the signal recorded (i.e., the energy deposited) in the scintillator elements is purely due to secondary x-ray photons and electrons arising from x-ray interactions within the walls. Thus, in the case of the polystyrene-based detector, the signal drops because relatively fewer x rays interact within the septa. The reverse effect occurs in the
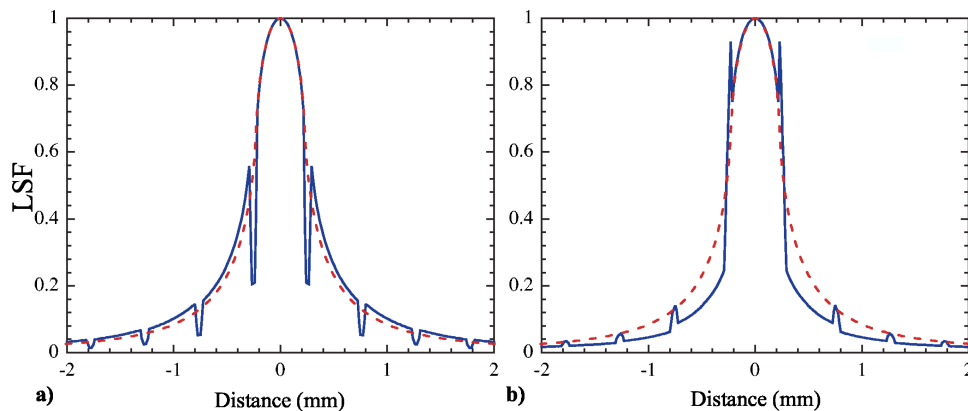

FIG. 5. Line spread functions obtained from Monte Carlo simulations of the angled-slit method for a 40 mm thick, CsI(T1)-based segmented detector incorporating 50 μm thick septa. The solid lines represent configurations employing (a) polystyrene and (b) tungsten septa. The dashed line in both figures corresponds to a LSF calculated for the same 40 mm thick CsI(T1) detector with "septa" composed of CsI(T1), thus making the detector a homogeneous slab. Note that, all LSFs have been normalized with respect to their peak values, in order to better illustrate comparisons between the homogeneous CsI(T1) slab and the segmented detectors.
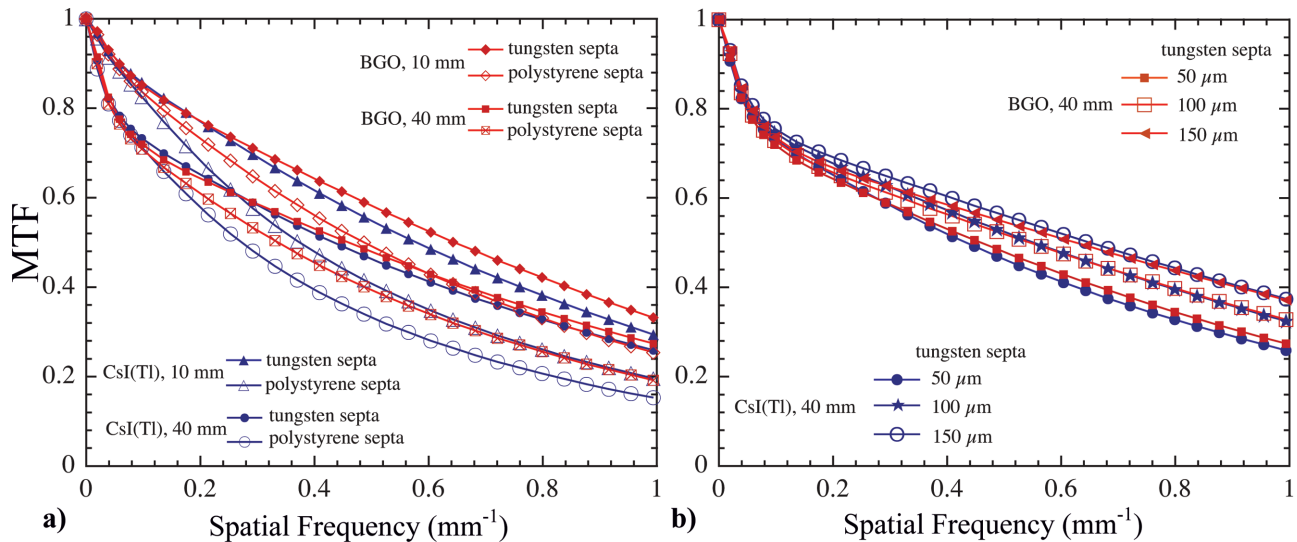
FIG. 6. (a) Monte Carlo-based theoretical calculations of MTF_{ID} for segmented detectors incorporating CsI(T1) and BGO scintillators with 10 and 40 mm tall elements and 50 μm thick, low-density (polystyrene) or high-density (tungsten) septal walls. (b) MTF_{ID} calculations for 40 mm thick CsI(T1) and BGO detectors incorporating 50, 100, and 150 μm thick tungsten septal walls.

tungsten-based configurations, giving rise to signal enhancements that are reflected as peaks in the LSF. In comparison, when the septa are replaced by CsI(Tl), the probability of x-ray interactions and energy deposition due to secondary radiation is the same for all positions of the incident beam. Therefore, the LSF shows a smooth curve, as would be expected for a homogeneous medium.

It should be noted that the LSF results shown in Fig. 5 differ considerably in shape from those for another segmented detector design described by Pang and Rowlands.[14] These differences in shape can probably be attributed to the fact that in the calculation shown in Pang and Rowlands, the LSF is proportional to the electron fluence. In contrast, the Monte Carlo-based approach adopted in this paper is solely based on the energy deposited within each detector element, which, in the context of the present work, is more representative of the physical processes involved in image formation.

Figure 6(a) shows MTF_{ID} curves for 10 and 40 mm tall CsI(Tl) and BGO segmented detectors incorporating 50 μm thick, polystyrene or tungsten septa. As expected (see Sec. II C 1), the 10 mm tall detectors exhibit superior MTF compared to corresponding 40 mm tall configurations. Detectors incorporating tungsten septa exhibit significantly higher MTF than corresponding configurations using polystyrene septa—likely due to the higher degree of cross talk in the latter, as discussed above. In addition, for detectors employing polystyrene, the MTF for configurations based on the higher density scintillator BGO is significantly superior to that of corresponding CsI(Tl) configurations. With the incorporation of tungsten septa, the MTF_{ID} is dominated by the septal walls and, for the taller detectors, becomes practically independent of the density of the scintillator material. This point is further illustrated in Fig. 6(b), which shows MTF_{ID} for 40 mm tall CsI(Tl) and BGO detectors incorporating progressively thicker tungsten septa. For both scintillators, MTF_{ID} is observed to improve with increasing wall thick-

ness. While some of this improvement can be attributed to the reduced scintillator fill factor (and consequently, higher aperture MTF), a significantly larger fraction of the improvement is due to a reduction in cross talk between adjacent scintillator elements. Moreover, the calculations strongly suggest that, for high-density septa, the spread of the absorbed energy is dominated by the septal walls, with both BGO and CsI(Tl)-based configurations exhibiting comparable MTF_{ID}.

3. Noise properties (NPS_{ID})

Figures 7(a) and 7(b) show the noise power spectra (NPS_{ID}) of the absorbed energy for the various segmented detector configurations shown in Fig 6. Both CsI(Tl) and BGO detectors using polystyrene septa exhibit a drop in the NPS at higher frequencies, indicating significant noise correlations over short distances. Such noise correlations occur due to the relatively lower spatial resolution of these detectors compared to those using tungsten septa [Fig. 6(a)], which exhibit a relatively flatter spectral response. As expected from the signal (Fig. 4) and the MTF results [Fig. 6(b)], in the case of detectors with thicker tungsten walls, the noise power spectra decrease in magnitude and flatten out with increasing wall thickness [Fig. 7(b)].

4. Intrinsic detector DQE (DQE_{ID})

Figure 8(a) shows DQE_{ID} for various detector configurations incorporating 50 μm thick septal walls, calculated from the Monte Carlo results shown in Figs. 6 and 7. In general, the DQE_{ID} improves with increasing detector thickness, detector density, and septal wall density. The following results are particularly noteworthy. First, the 10 mm thick BGO detector incorporating tungsten septa exhibits DQE_{ID} comparable and, at higher spatial frequencies even superior, to that of a 40 mm thick CsI(Tl) detector incorporating polystyrene
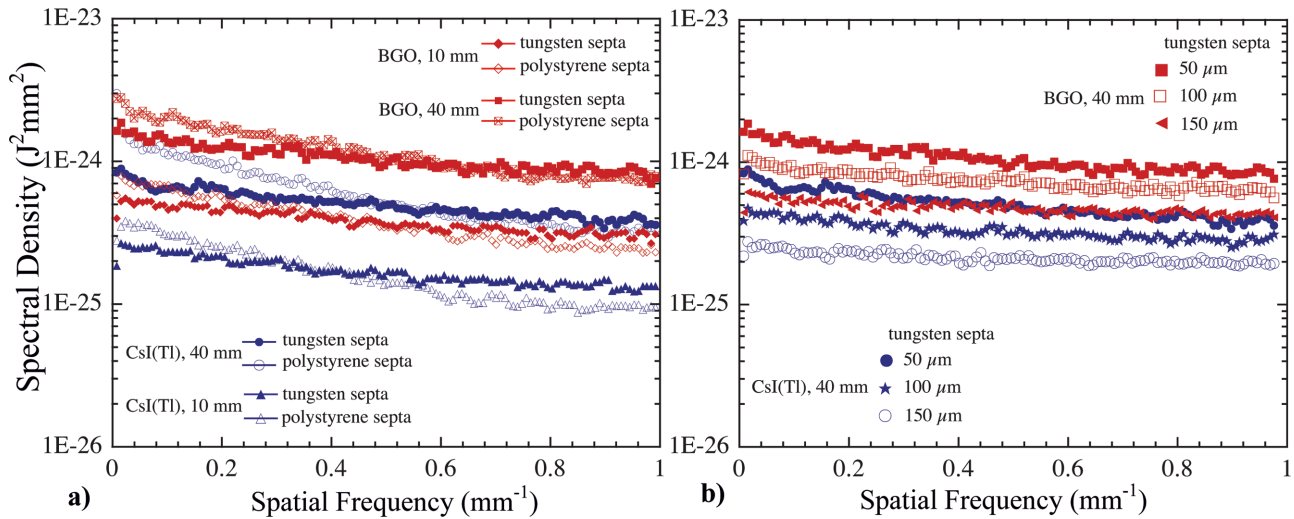
FIG. 7. Noise power characteristics of the absorbed energy corresponding to the various segmented detector configurations of (a) Fig. 6(a) and (b) Fig. 6(b). Note that the symbols used in (a) and (b) in the present figure are consistent with those used in Figs. 6(a) and 6(b), respectively.

septa. Second, with the incorporation of tungsten septa, the 40 mm thick CsI(Tl) detector exhibits DQE_{ID} approaching that of the 40 mm thick BGO+polystyrene configuration.

Interestingly, although the 40 mm thick detectors show higher absorbed energy per voxel when incorporating polystyrene as opposed to tungsten septal walls (Fig. 4), the tungsten-based configurations exhibit significantly superior DQE_{ID} across the entire frequency range. This indicates that the signal "enhancement" achieved by using low-density septal walls comes at the cost of significantly increased noise—a fact that can also be observed from the NPS_{ID} results shown in Fig. 7(a). The decreased noise in the case of tungsten-based configurations may be due to relatively higher absorption of low-energy x-ray photons and electrons within the tungsten septa. Consequently, the absorbed energy distribution (AED) (Ref. 60) within the scintillator elements will be narrower for tungsten-based detector configurations compared to the corresponding polystyrene-based detectors. A narrower AED results in lower Swank noise of the energy absorption process,[61] which is an important determinant of the DQE—since the zero-frequency DQE is given by the product of the x-ray quantum efficiency and the Swank factor.[62]

From the above results, it appears that high-density septal walls are highly desirable for segmented crystalline detectors. However, further increases in the thickness of high-density septa do not necessarily improve the DQE. This is illustrated in Figs. 8(b) and 8(c) which show DQE_{ID} for 40 mm thick BGO and CsI(Tl) detectors, respectively, incorporating 50 to 150 μm thick tungsten septa. For both scintillators, the low-frequency DQE_{ID} decreases with increasing wall thickness—an effect likely due to the smaller signal generated as a result of the reduced scintillator fill factor (Fig. 4). At higher frequencies, the DQE_{ID} for BGO detectors is observed to decrease slightly with increasing wall thickness, while in the case of the lower density CsI(Tl) detectors,

there is a slight enhancement of the high-frequency DQE_{ID} for detectors incorporating thicker walls due to improvements in their respective MTFs [Fig. 6(b)].

C. X-ray sensitivity

Figure 9(a) shows a profile of the x-ray sensitivity obtained from a central region of the prototype detector coupled to a 100×100 pixel region of the 127 μm pitch active matrix array. For comparison, a sensitivity profile from the same array pixels obtained using a Lanex Fast-B screen, obtained under identical measurement conditions, is shown in Fig. 9(b). As a result of over-sampling the CsI(Tl) detector voxels (1 mm pitch), the response of individual voxels can be observed, with the center of each voxel exhibiting a peak response that gradually falls off toward the septa. All voxels exhibit similar signal response, indicating good voxel-to-voxel uniformity. In addition, the individual peaks are well-delineated, indicating good optical isolation between adjacent voxels and good optical coupling between the detector and the active matrix array. Finally, contrary to expectations, the prototype detector shows lower x-ray sensitivity than Lanex Fast-B. Monte Carlo-based theoretical calculations indicate that a 2 mm thick CsI(Tl) scintillator (with 1 mm Cu buildup) exhibits a QE of $\sim$7% for a 6 MV spectrum, compared to $\sim$2% for a Lanex Fast-B+1 mm Cu combination. Since both CsI(Tl) and Gd_2O_2S:Tb exhibit comparable light output per unit absorbed energy,[62] the x-ray sensitivity of CsI(Tl) should be higher than that exhibited by Lanex Fast-B. It is likely that the relatively poorer x-ray sensitivity of this early prototype is due to the presence of the optically absorptive layer on the Cu plate (see Sec. III C), as well as due to lower light output of the scintillator, which is likely caused by the introduction of impurities during the process of CsI(Tl) injection into the tungsten matrix.
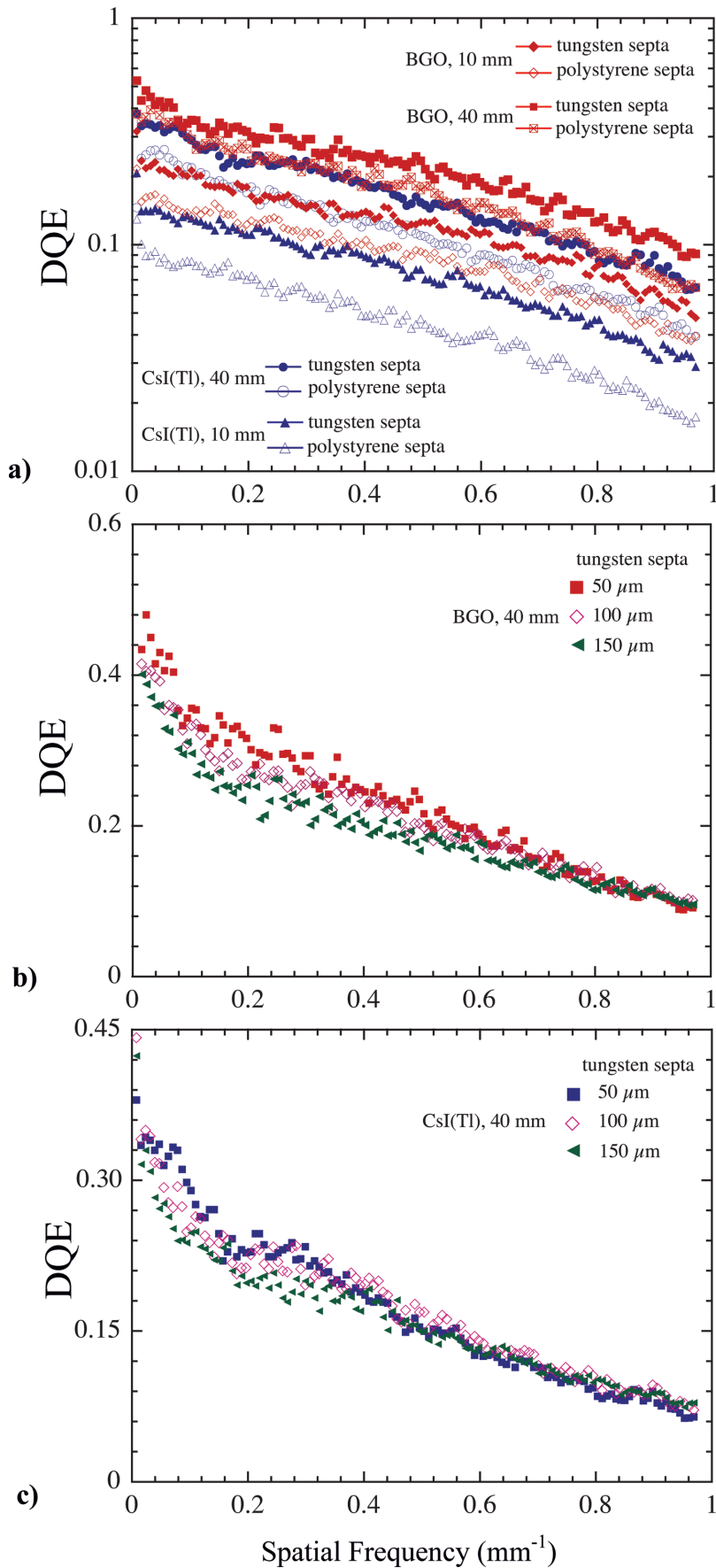
FIG. 8. (a) DQE upper limits corresponding to the segmented detector configurations of Fig. 6(a). Also shown are DQE upper limits for (b) BGO and (c) CsI(T1) segmented detectors incorporating increasingly thicker tungsten walls.
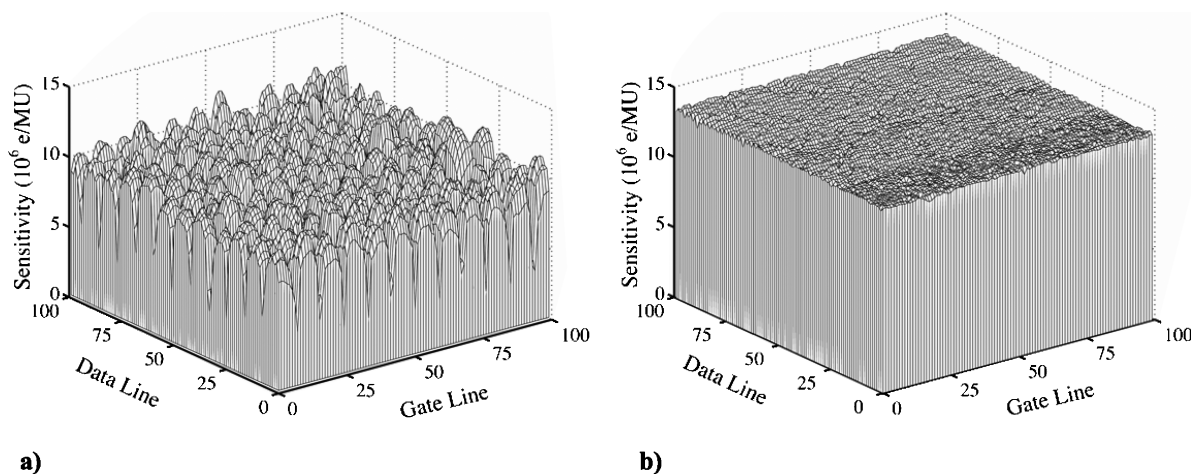
FIG. 9. (a) X-ray sensitivity profile from a central region of the prototype CsI(T1) segmented detector overlying a 100×100 pixel region of a 127 μm pitch indirect detection active matrix array. (b) Sensitivity profile obtained from the same 100×100 pixel with the array coupled to a Lanex Fast-B screen under identical measurement conditions.

However, it is important to note that lower light output is not necessarily a disadvantage in most megavoltage imagers. In fact, commercially available AMFPI EPIDs using phosphor screens similar to Lanex Fast-B employ an optically absorbent filter to attenuate a significant fraction of the emitted light, in order to avoid saturation of the photodiodes of the active matrix array pixels.[63] Thus while a sufficient amount of optical gain is necessary in order to ensure x-ray quantum limited operation, further improvement in DQE can occur mainly through increases in the x-ray quantum efficiency.

V. DISCUSSION

The last few years have witnessed a rapid increase in the adoption of image-guided techniques in virtually every aspect of radiotherapy[64] including numerous approaches that have been undertaken with the goal of obtaining images with soft-tissue contrast in the treatment room itself.[23,64–73] Of particular note, is the development of systems comprising a diagnostic (i.e., kV) x-ray source+AMFPI mounted on the gantry, orthogonal to the treatment beam direction.[23,69,70] These systems, capable of yielding high-contrast, diagnostic quality projection and tomographic images, have recently been made commercially available—which is a strong indicator of the desire within the radiotherapy community to be able to clearly delineate the tumor volume immediately prior to, and perhaps even during, dose delivery.

Notwithstanding the promising results shown by such systems, there exist strong incentives for the development of high-DQE megavoltage imagers capable of resolving soft-tissue contrast at very low doses. For example, projection and tomographic images obtained from the treatment beam itself would eliminate potential geometric uncertainties that could occur with an orthogonally mounted kV system. Also eliminated would be the expense and effort associated with the purchase, maintenance, and quality assurance of such additional equipment. Moreover, MVCT images could potentially yield more accurate information for radiotherapy dose

calculations and inhomogeneity corrections.[74–76] Finally, megavoltage CT images are largely insensitive to metal objects present in the volume imaged (such as dental fillings, hip prostheses, etc.)—as opposed to kV CT images, which exhibit significant streak artifacts under such conditions.[24]

Although soft-tissue contrast in megavoltage tomographic images has been demonstrated using conventional AMFPI systems incorporating phosphor screen-based detectors, the low x-ray quantum efficiency and, consequently, low DQE of these devices largely precludes their use for MVCT at clinically practical doses.[23] From the empirical and theoretical results presented in this work, it can be seen that AMFPIs based on thick, segmented, crystalline detectors show strong potential for overcoming this constraint.

Obviously, the practical development and incorporation of such detectors into clinical megavoltage imagers requires many issues to be addressed. For example, it is expected that light photons generated on the x-ray side of the detector are likely to undergo significantly more reflection and absorption events before reaching the pixel photodiode, compared to those generated nearer to the active matrix array. This effect becomes more pronounced as the thickness and/or the aspect ratio of the elements increases, and gives rise to a depth-dependent optical gain (and consequently, increased Swank noise) which can significantly degrade the DQE.[27] In order to minimize such depth-dependent optical gain, it is critical to maintain high reflectivity of the septal walls and choose a scintillator that exhibits high light transmission. In this regard, the two scintillators examined in the present study have been shown to exhibit such high optical transmission, both in bulk form[43,47,51,52] and in the segmented crystal form.[77] In particular, segmented crystals of BGO exhibit more than 80% transmission over an optical path length of 40 mm.[77] Although CsI(Tl) exhibits slightly lower transmission (between 50% and 80% over a 40 mm path length, depending upon the manufacturer),[43,51,52] it is likely that, with the high light output of this scintillator ($\sim$61 000 photons/MeV),[59]
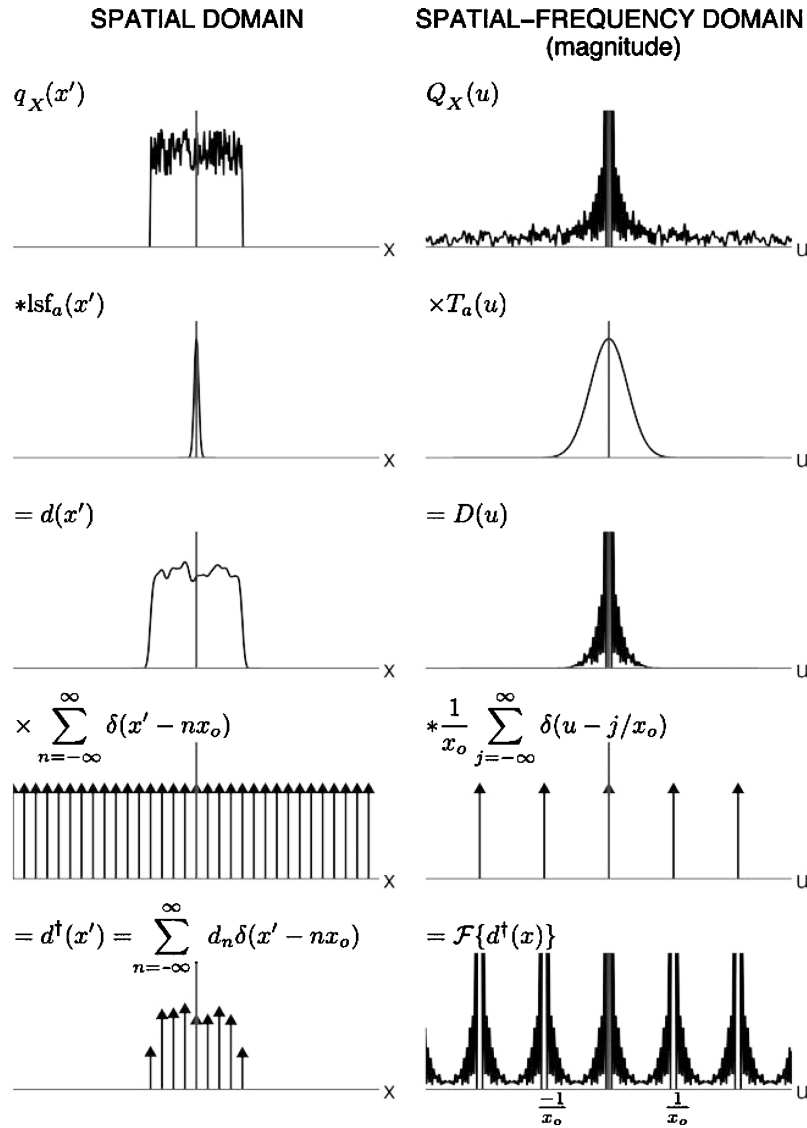
SPATIAL DOMAIN   **SPATIAL–FREQUENCY DOMAIN (magnitude)**

$q_X(x')$ $Q_X(u)$

$*\mathrm{lsf}_a(x')$ $\times T_a(u)$

$= d(x')$ $= D(u)$

$$\times \sum_{n=-\infty}^{\infty} \delta(x' - nx_o)$$ $$*\frac{1}{x_o} \sum_{j=-\infty}^{\infty} \delta(u - j/x_o)$$

$$= d^\dagger(x') = \sum_{n=-\infty}^{\infty} d_n \delta(x' - nx_o)$$ $$= \mathcal{F}\{d^\dagger(x)\}$$

$\frac{-1}{x_o}$ $\frac{1}{x_o}$

FIG. 10. A one-dimensional schematic illustration of the various steps involved in the derivation of the LSF and presampling MTF for a segmented detector. The left and right columns correspond to the spatial and the spatial-frequency domains, respectively.

the noise contribution due to self-absorption of light will be small compared to that due to the variance in the absorbed energy

As detector thickness increases beyond ∼10 mm, it becomes necessary to "focus" the elements toward the x-ray source (see Fig. 1) in order to avoid loss of spatial resolution in detector regions away from the central axis. It is estimated that these effects may cause up to 15% reduction in MTF at the periphery of large fields (e.g., 40×40 cm^2 at isocenter) for the thickest detectors examined in this study. Current segmented detector fabrication techniques, such as the one described in this work (Sec. III C) or those that involve dicing single-crystal blocks and infusing septal material within the gaps,[18,28] will have to be suitably modified in order to create focused detectors. As these fabrication challenges are expected to be nontrivial, it is possible that some tradeoff may be required between spatial resolution at field edges and x-ray quantum efficiency.

In summary, the considerations described above, along with the theoretical results, appear to strongly favor the use of high-density scintillator and septal wall materials. More-over, our results suggest that a thinner high-density scintillator can be used to achieve the same quantum efficiency (and conceivably, superior DQE), compared to a thicker, lower-density scintillator, thus mitigating various adverse effects that occur with increasing scintillator thickness. In this regard, scintillators such as CdWO$_4$ and ZnWO$_4$ (densities 7.9 and 7.62 g/cm^3, respectively) and recently developed very high-density (9.4 g/cm^3) ceramic scintillators[78,79] appear to be attractive candidates.

VI. CONCLUSION

This work represents an initial, systematic, theoretical, and empirical investigation of segmented crystalline scintillator-based detectors for megavoltage x-ray imaging. The results of this study indicate that such detectors show good potential for improving the DQE of megavoltage AM-FPIs by over an order of magnitude. While the practical realization of such devices requires the careful consideration and optimization of many parameters, as well as the development of novel fabrication techniques, it is strongly antici-

pated that the segmented detector approach can provide a viable pathway toward the realization of very high-performance megavoltage x-ray imagers, capable of providing soft-tissue contrast at clinically acceptable doses in megavoltage tomographic and, perhaps, even projection imaging.

ACKNOWLEDGMENTS

APPENDIX

A segmented detector is a shift-variant system. While in a strict sense this fails the shift-invariant prerequisite for use of Fourier-based metrics such as MTF, NPS, and DQE, it is shown here that Fourier methods can still be used with some qualifications. In particular, we consider a segmented detector coupled to an underlying, element-matched, indirect detection-based active matrix photodiode array and show that concepts of presampling MTF and aliasing apply as they do for uniform-scintillator-based imagers such as conventional AMFPIs, CCD camera-based systems, etc.

In such a configuration, the elements of the segmented detector are registered to the photodiode elements and therefore, light emitted from a detector element is incident only on the underlying photodiode element. The photodiode array elements are assumed to have unity optical fill factor and be perfectly optically coupled to the segmented detector (i.e., all of the optical photons exiting a detector element are incident on the underlying array element).

Let (x_0, y_0) be the center-to-center spacing of the detector elements (and also that of the array elements). The signal obtained from each array element is proportional to the total number of optical photons absorbed within that element

$$d_{n,m} = k\eta q_{n,m}, \tag{A1}$$

where $d_{n,m}$ is the output signal from the (n,m)th array element, $q_{n,m}$ is the total number of optical photons incident on the array element (equal to the number of optical photons exiting the overlying segmented detector element), η is the light collection efficiency of the photodiode (~ 0.65 for typical active matrix photodiode arrays), and k is a constant of proportionality. The distribution of optical quanta emitted by the scintillator will not be uniform due, in part, to the segmented-detector structure, and therefore $q_{n,m}$ represents

an integral of the spatial distribution of optical quanta emitted across the (n,m)th element

$$q_{n,m} = \int_{x''=nx_0-x_0/2}^{nx_0+x_0/2} \int_{y''=my_0-y_0/2}^{my_0+y_0/2} q_{opt}(x'', y'') dx'' dy'' \tag{A2}$$

where $q_{opt}(x'', y'')$ is the distribution of optical quanta as a function of position (x'', y'') on the segmented detector in units of mm^{-2}. (The double-prime notation is chosen for later convenience.)

Optical quanta emitted at (x'', y'') result from x-ray interactions that take place near that point (x-ray scatter and electron transport will result in a redistribution where energy is absorbed and thereby, optical quanta produced). Thus, if $q_X(x', y')$ describes the spatial distribution of x-ray quanta [mm^{-2}] with energy $h\nu$ incident on the detector at (x', y') and $p(x'', y'', x', y')$ describes the probability density that x-ray energy incident at (x', y') is *ultimately* absorbed at (x'', y''), the spatial distribution of optical quanta *exiting* the segmented detector can be written as

$$q_{opt}(x'', y'') = \frac{h\nu}{W_{eff}} \int_{-\infty}^{\infty} \int_{-\infty}^{\infty} q_X(x', y') p(x'', y'', x', y') dx' dy', \tag{A3}$$

where $h\nu$ is the energy of the incident x-ray photon and W_{eff} is the "effective" work function of the segmented detector and represents the average amount of energy absorbed per *exiting* light photon. (Thus, W_{eff} is different from the single-crystal work function W, which is defined as the average energy required to *generate* an optical photon.) For any specified value of (x', y'), $p(x'', y'', x', y')$ has units of mm^{-2}, is normalized to unity area, and is dependent on the geometry of the segmented detector. The signal from the (n,m)-th photodiode array element, $d_{n,m}$, is therefore given by

$$d_{n,m} = k\eta \frac{h\nu}{W_{eff}} \int_{x''=nx_0-x_0/2}^{nx_0+x_0/2} \int_{y''=my_0-y_0/2}^{my_0+y_0/2} \int_{x'=-\infty}^{\infty} \int_{y'=-\infty}^{\infty}$$
$$\times q_X(x', y') p(x'', y'', x', y') dx' dx'' dy' dy'', \tag{A4}$$

which can be rewritten as

$$d_{n,m} = k\eta \frac{h\nu}{W_{eff}} \int_{x'=-\infty}^{\infty} \int_{y'=-\infty}^{\infty} q_X(x', y') \int_{x''=nx_0-x_0/2}^{nx_0+x_0/2}$$
$$\times \int_{y''=my_0-y_0/2}^{my_0+y_0/2} p(x'', y'', x', y') dx'' dy'' dx' dy'. \tag{A5}$$

The nested integral over (x'', y'') represents the spatial integration of optical quanta by the (n,m)-th array element and gives the relative response of that element to x rays at (x', y'), which is simply the response function (sensitivity profile) of that element to a small x-ray beam being scanned across the entire detector. Since all detector elements are identical and are exactly registered with photodiode array elements, this profile is a function of distance between (x', y') and the element centers only and is the same for each element. We choose to express it as $p_a(nx_0 - x', my_0 - y')$, the

aperture response function for the element centered at (nx_0, my_0)

$$p_a(nx_0 - x', my_0 - y') = \int_{x''=nx_0-x_0/2}^{nx_0+x_0/2} \int_{y''=my_0-y_0/2}^{my_0+y_0/2}$$
$$\times p(x'', y'', x', y') dx'' dy''. \quad (A6)$$

Substitution into Eq. (A5) gives the output from the (n, m)-th, element as

$$d_{n,m} = k\eta \frac{h\upsilon}{W_{\text{eff}}} \int_{x'=-\infty}^{\infty} \int_{y'=-\infty}^{\infty}$$
$$\times q_X(x', y') p_a(nx_0 - x', my_0 - y') dx' dy', \quad (A7)$$

which has physical meaning for integer values of n and m only. It is convenient to express $d_{n,m}$ as

$$d_{n,m} = d(x, y)\big|_{x,y=nx_0,my_0}, \quad (A8)$$

where

$$d(x, y) = k\eta \frac{h\upsilon}{W_{\text{eff}}} \int_{x'=-\infty}^{\infty} \int_{y'=-\infty}^{\infty}$$
$$\times q_X(x', y') p_a(x - x', y - y') dx' dy'. \quad (A9)$$

The double integral is recognized as being a two-dimensional convolution of $q_X(x, y)$ with $p_a(x, y)$, and hence

$$d(x, y) = k\eta \frac{h\upsilon}{W_{\text{eff}}} \times q_X(x, y) ** p_a(x, y)\bigg|_{x,y=nx_0,my_0}, \quad (A10)$$

where $**$ represents a 2D convolution operator and $d(x, y)$ is called the *detector presampling signal*. It is a function that, when evaluated at (x, y), gives the output signal for an element centered at that position. It therefore has physical meaning only for $(x, y) = (nx_0, my_0)$, corresponding to the physical elements of the detector. At other locations, it gives the signal that an element would have if centered at that position.

All steps in the above derivation can be represented in terms of a cascade of linear processes as illustrated in Fig. 10 in both the spatial (left column) and spatial-frequency (right column) domains. This formalism is useful as it illustrates two things. First, it shows that, similar to a digital detector based on a homogeneous scintillator, the output signal can be expressed in terms of a presampling signal in the spatial domain and therefore a presampling MTF and sampling frequency in the Fourier domain. It is important to note that, this *only* occurs because scintillator elements are registered to the photodiode array elements and the point spread function therefore can be written as a function of distance from the element centers only. Second, the presampling MTF of the detector is easily recognized as being $|T_a(u)|$, the modulus of the Fourier transform of the line-spread function $\text{LSF}_a(x)$

$$\text{LSF}_a(x) = \int_{y=-\infty}^{\infty} p_a(x, y) dy. \quad (A11)$$

As explained in Sec. III B 2, we evaluate the LSF through a Monte Carlo calculation that simulates the angled slit technique (Ref. 56).

[a)]Electronic mail: asawant@umich.edu

[1]L. E. Antonuk, "Electronic portal imaging devices: A review and historical perspective of contemporary technologies and research," Phys. Med. Biol. **47**, R31–R65 (2002).

[2]L. E. Antonuk *et al.*, "Initial performance evaluation of an indirect-detection, active matrix flat-panel imager (AMFPI) prototype for megavoltage imaging," Int. J. Radiat. Oncol., Biol., Phys. **42**, 437–454 (1998).

[3]J. J. Kruse *et al.*, "Electronic and film portal images: A comparison of landmark visibility and review accuracy," Int. J. Radiat. Oncol., Biol., Phys. **54**, 584–591 (2002).

[4]P. Munro and D. C. Bouius, "X-ray quantum limited portal imaging using amorphous silicon flat-panel arrays," Med. Phys. **25**, 689–702 (1998).

[5]Y. El-Mohri, K.-W. Jee, L. E. Antonuk, M. Maolinbay, and Q. Zhao, "Determination of the detective quantum efficiency of a prototype, megavoltage indirect detection, active matrix flat-panel imager," Med. Phys. **28**, 2538–2550 (2001).

[6]J.-P. Bissonnette, I. A. Cunningham, and P. Munro, "Optimal phosphor thickness for portal imaging," Med. Phys. **24**, 803–814 (1997).

[7]F. Cremers *et al.*, "Performance of electronic portal imaging devices (EPIDs) used in radiotherapy: Image quality and dose measurements," Med. Phys. **31**, 985–996 (2004).

[8]E. Samei and M. J. Flynn, "An experimental comparison of detector performance for direct and indirect digital radiography systems," Med. Phys. **30**, 608–622 (2003).

[9]E. Samei, M. J. Flynn, H. G. Chotas, and J. T. Dobbins, "DQE of direct and indirect digital radiographic systems," Proc. SPIE **4320**, 189–197 (2001).

[10]P. R. Granfors and R. Aufrichtig, "Performance of a 41X41-cm2 amorphous silicon flat panel x-ray detector for radiographic imaging applications," Med. Phys. **27**, 1324–1331 (2000).

[11]D. L. Lee *et al.*, "Filtered gain calibration and its effect on frequency-dependent DQE and image quality in SE-based general radiography and full-field mammographic digital imaging," Proc. SPIE **4320**, 121–126 (2001).

[12]G. Pang and J. A. Rowlands, "Development of high quantum efficiency flat panel detectors for portal imaging: Intrinsic spatial resolution," Med. Phys. **29**, 2274–2285 (2002).

[13]E. J. Seppi *et al.*, "Megavoltage cone-beam computed tomography using a high-efficiency image receptor," Int. J. Radiat. Oncol., Biol., Phys. **55**, 793–803 (2003).

[14]G. Pang and J. A. Rowlands, "Development of high quantum efficiency, flat panel, thick detectors for megavoltage x-ray imaging: A novel direct-conversion design and its feasibility," Med. Phys. **31**, 3004–3016 (2004).

[15]F. DiBianca, S. Samant, J. Laughter, J. Rasmussen, and C. Rodriguez, "Use of a kinestatic charge detector for megavoltage portal imaging," *Proceedings of SPIE Conference on Physics of Medical Imaging*, Vol. 3032 (1997), pp. 195–201.

[16]C. Iacobaeus *et al.*, "A novel portal imaging device for advanced radiation therapy," IEEE Trans. Nucl. Sci. **48**, 1496–1502 (2001).

[17]T. T. Monajemi, S. Steciw, B. G. Fallone, and S. Rathee, "Modeling scintillator-photodiodes as detectors for megavoltage CT," Med. Phys. **31**, 1225–1234 (2004).

[18]M. A. Mosleh-Shirazi *et al.*, "Rapid portal imaging with a high-efficiency, large field-of-view detector," Med. Phys. **25**, 2333–2346 (1998).

[19]J. Ostling *et al.*, "Novel detector for portal imaging in radiation therapy," *Proceedings of SPIE Conference on Physics of Medical Imaging*, Vol. 3977 (2000), pp. 84–95.

[20]A. Sawant *et al.*, "Theoretical analysis and experimental evaluation of a CsI(Tl) based electronic portal imaging system," Med. Phys. **29**, 1042–1053 (2002).

[21]B. Wowk and S. Shalev, "Thick phosphor screens for on-line portal imaging," Med. Phys. **21**, 1269–1276 (1994).

[22]B. Wowk, S. Shalev, and T. Radcliffe, "Grooved phosphor screens for online portal imaging," Med. Phys. **20**, 1641–1651 (1993).

[23]B. A. Groh, J. H. Siewerdsen, D. G. Drake, J. W. Wong, and D. A. Jaffray, "A performance comparison of flat-panel imager-based MV and kV cone-beam CT," Med. Phys. **29**, 967–975 (2002).

[24]F. A. Ghelmansarai *et al.*, "Soft tissue visualization using a highly efficient megavoltage cone beam CT imaging system," Proc. SPIE **5745**, 159–170 (2005).

[25]H. Keller *et al.*, "Monte Carlo study of a highly efficient gas ionization detector for megavoltage imaging and image-guided radiotherapy," Med. Phys. **29**, 165–175 (2002).

[26]K. M. Langen and D. T. Jones, "Organ motion and its management," Int. J. Radiat. Oncol., Biol., Phys. **50**, 265–278 (2001).

[27]A. Sawant *et al.*, "Segmented phosphors: MEMS-based high quantum efficiency detectors for megavoltage x-ray imaging," Med. Phys. **32**, 553–565 (2005).

[28]M. A. Mosleh-Shirazi, W. Swindell, and P. M. Evans, "Optimization of the scintillation detector in a combined 3D megavoltage CT scanner and portal imager," Med. Phys. **25**, 1880–1890 (1998).

[29]A. Badano and R. Leimbach, "Depth-dependent phosphor blur in indirect x-ray imaging sensors," Proc. SPIE **4682**, 94–106 (2002).

[30]A. Badano *et al.*, "Lubberts effect in columnar phosphors," Med. Phys. **31**, 3122–3131 (2004).

[31]M. Albert and A. D. Maidment, "Linear response theory for detectors consisting of discrete arrays," Med. Phys. **27**, 2417–2434 (2000).

[32]I. Cunningham, "Applied linear-systems theory," in *Handbook of Medical Imaging*, edited by J. Beutel, H. L. Kundel, and R. L. Van Metter (SPIE Press, Bellingham, Washington, 2000), pp. 79–159.

[33]M. L. Giger and K. Doi, "Investigation of basic imaging properties in digital radiography. I: Modulation transfer function," Med. Phys. **11**, 287–295 (1984).

[34]A. Papoulis, *Probability, Random-Variables, and Stochastic-Processes*, 3rd ed. (McGraw Hill, New York, 1991).

[35]W. A. Gardner and L. E. Franks, "Characterization of cyclostationary random signal processes," IEEE Trans. Inf. Theory **IT21**, 4–14 (1975).

[36]I. A. Cunningham, M. Sattarivand, G. Hajdok, and J. Yao, "Can a Fourier-based cascaded-systems analysis describe noise in complex shift-variant spatially sampled detectors?" Proc. SPIE **5368**, 79–88 (2004).

[37]J. T. Dobbins, "Image quality metrics for digital systems," in *Handbook of Medical Imaging*, edited by J. Beutel, H. L. Kundel, and R. L. Van Metter (SPIE Press, Bellingham, Washington, 2000), pp. 163–222.

[38]J. C. Dainty and R. Shaw, *Image Science—Principles, Analysis and Evaluation of Photographic-Type Imaging Processes* (Academic Press, New York, 1974).

[39]M. Rabbani, R. Shaw, and R. Van Metter, "Detective quantum efficiency of imaging systems with amplifying and scattering mechanisms," J. Opt. Soc. Am. A **4**, 895–901 (1987).

[40]I. A. Cunningham, M. S. Westmore, and A. Fenster, "A spatial-frequency dependent quantum accounting diagram and detective quantum efficiency model of signal and noise propagation in cascaded imaging systems," Med. Phys. **21**, 417–427 (1994).

[41]A. R. Sawant *et al.*, "Exploring new frontiers in x-ray quantum limited portal imaging using active matrix flat-panel imagers (AMFPIs)", *Proceedings of SPIE Conference on the Physics of Medical Imaging*, Vol. 5030, pp. 478–489 (2003).

[42]R. Y. Zhu, D. A. Ma, and H. Newman, "Scintillating crystals in a radiation environment," Nucl. Phys. B 547–556 (1995).

[43]R. Y. Zhu, "Radiation damage in scintillating crystals," Nucl. Instrum. Methods Phys. Res. A **413**, 297–311 (1998).

[44]S. K. Sahu *et al.*, "Radiation hardness of undoped BGO crystals," Nucl. Instrum. Methods Phys. Res. A **388**, 144–148 (1997).

[45]R. Georgii *et al.*, "Influence of radiation damage on BGO scintillation properties," Nucl. Instrum. Methods Phys. Res. A **413**, 50–58 (1998).

[46]K. C. Peng *et al.*, "Low-dose radiation damage and recovery of undoped BGO crystals," Nucl. Instrum. Methods Phys. Res. A **452**, 252–255 (2000).

[47]P. Kozma and P. Kozma, "Radiation resistivity of BGO crystals due to low-energy gamma-rays," Nucl. Instrum. Methods Phys. Res. A **501**, 499–504 (2003).

[48]M. A. H. Chowdhury, A. Holmes-Siedle, A. K. McKemey, S. J. Watts, and D. C. Imrie, "Radiation effects in CsI(Tl) crystals from a controlled growth process," Nucl. Instrum. Methods Phys. Res. A **413**, 471–474 (1998).

[49]M. A. H. Chowdhury, S. J. Watts, D. C. Imrie, A. K. McKemey, and A. G. Holmes-Siedle, "Studies of radiation tolerance and optical absorption bands of CsI(Tl) crystals," Nucl. Instrum. Methods Phys. Res. A **432**, 147–156 (1999).

[50]M. M. Hamada, F. E. Costa, S. Shimizu, and S. Kubota, "Radiation damage of CsI(Tl) scintillators: Blocking of energy transfer process of V-k centers to Tl+ activators," Nucl. Instrum. Methods Phys. Res. A **486**, 330–335 (2002).

[51]K. Kazui *et al.*, "Study of the radiation hardness of CsI(Tl) crystals for the BELLE detector," Nucl. Instrum. Methods Phys. Res. A **394**, 46–56 (1997).

[52]C. L. Woody, J. A. Kierstead, P. W. Levy, and S. Stoll, "Radiation-damage in undoped CsI and CsI(Tl)," IEEE Trans. Nucl. Sci. **39**, 524–531 (1992).

[53]I. Kawrakow and D. W. O. Rogers, "The EGSnrc code system: Monte Carlo simulation of electron and photon transport," Technical Report PIRS-701, National Research Council of Canada, Ottawa, Canada 2000.

[54]J. A. Treurniet, B. R. B. Walters, and D. W. O. Rogers, "BEAMnrc, DOSXYZnrc and BEAMDP GUI user's manual," NRC Report PIRS 0623(rev B) (2001).

[55]D. Sheikh-Bagheri, "Monte Carlo study of photon beams from medical linear accelerators: Optimization, benchmark and spectra," Ph.D. thesis, Dept. of Physics, Carleton University, 1999.

[56]H. Fujita *et al.*, "A simple method for determining the modulation transfer-function in digital radiography," IEEE Trans. Med. Imaging **11**, 34–39 (1992).

[57]J. H. Siewerdsen *et al.*, "Signal, noise power spectrum, and detective quantum efficiency of indirect-detection flat-panel imagers for diagnostic radiology," Med. Phys. **25**, 614–628 (1998).

[58]L. E. Antonuk *et al.*, "Empirical investigation of the signal performance of a high-resolution, indirect detection, active matrix flat-panel imager (AMFPI) for fluoroscopic and radiographic operation," Med. Phys. **24**, 51–70 (1997).

[59]M. Moszynski, M. Kapusta, M. Mayhugh, D. Wolski, and S. O. Flyckt, "Absolute light output of scintillators," IEEE Trans. Nucl. Sci. **44**, 1052–1061 (1997).

[60]D. A. Jaffray, J. J. Battista, A. Fenster, and P. Munro, "Monte-Carlo studies of x-ray-energy absorption and quantum-noise in megavoltage transmission radiography," Med. Phys. **22**, 1077–1088 (1995).

[61]R. K. Swank, "Absorption and noise in x-ray phosphors," J. Appl. Phys. **44**, 4199–4203 (1973).

[62]J. A. Rowlands and J. Yorkston, "Flat panel detectors for digital radiography," in *Handbook of Medical Imaging*, edited by J. Beutel, H. L. Kundel, and R. L. Van Metter (SPIE Press, Bellingham, Washington, 2000), pp. 223–328.

[63]C. Kirkby and R. Sloboda, "Comprehensive Monte Carlo calculation of the point spread function for a commercial a-Si EPID," Med. Phys. **32**, 1115–1127 (2005).

[64]T. R. Mackie *et al.*, "Image guidance for precise conformal radiotherapy," Int. J. Radiat. Oncol., Biol., Phys. **56**, 89–105 (2003).

[65]J. L. Barker *et al.*, "Quantification of volumetric and geometric changes occuring during fractionated radiotherapy for head-and-neck cancer using an integrated CT/linear accelerator system," Int. J. Radiat. Oncol., Biol., Phys. **59**, 960–970 (2004).

[66]K. Kuriyama *et al.*, "A new irradiation unit constructed of self-moving gantry-CT and linac," Int. J. Radiat. Oncol., Biol., Phys. **55**, 428–435 (2003).

[67]J. M. Balter *et al.*, "Daily targeting of intrahepatic tumors for radiotherapy," Int. J. Radiat. Oncol., Biol., Phys. **52**, 266–271 (2002).

[68]D. A. Jaffray, K. Chawla, C. Yu, and J. W. Wong, "Dual-beam imaging for online verification of radiotherapy field placement," Int. J. Radiat. Oncol., Biol., Phys. **33**, 1273–1280 (1995).

[69]D. A. Jaffray, D. G. Drake, M. Moreau, A. A. Martinez, and J. W. Wong, "A radiographic and tomographic imaging system integrated into a medical linear accelerator for localization of bone and soft-tissue targets," Int. J. Radiat. Oncol., Biol., Phys. **45**, 773–789 (1999).

[70]D. A. Jaffray, J. H. Siewerdsen, J. W. Wong, and A. A. Martinez, "Flat-panel cone-beam computed tomography for image-guided radiation therapy," Int. J. Radiat. Oncol., Biol., Phys. **53**, 1337–1349 (2002).

[71]J. Lattanzi, S. McNeeley, A. Hanlon, T. E. Schultheiss, and G. E. Hanks, "Ultrasound-based stereotactic guidance of precision conformal external beam radiation therapy in clinically localized prostate cancer," Urology **55**, 73–78 (2000).

[72]K. M. Langen *et al.*, "Evaluation of ultrasound-based prostate localization for image-guided radiotherapy," Int. J. Radiat. Oncol., Biol., Phys. **57**,

635–644 (2003).

[73] S. L. Meeks *et al.*, "Ultrasound-guided extracranial radiosurgery: Technique and application," Int. J. Radiat. Oncol., Biol., Phys. **55**, 1092–1101 (2003).

[74] R. G. Simpson, C. T. Chen, E. A. Grubbs, and W. Swindell, "A 4-MV CT scanner for radiation therapy: The prototype system," Med. Phys. **9**, 574–579 (1982).

[75] W. Swindell, R. G. Simpson, J. R. Oleson, C. Chen, and E. A. Grubbs, "Computed tomography with a linear accelerator with radiotherapy applications," Med. Phys. **10**, 416–420 (1983).

[76] A. Brahme, "Design principles and clinical possibilities with a new generation of radiation therapy equipment," Acta Oncol. **26**, 403–412 (1987).

[77] D. J. Krus, W. P. Novak, and L. Perna, "Precision linear and two-dimensional scintillation crystal arrays for x-ray and gamma-ray imaging applications," *Proc. SPIE on Hard X-Ray, Gamma-Ray, and Neutron Detector Physics*, Vol. 3768 (1999), pp. 183–194.

[78] A. Lempicki *et al.*, "A new lutetia-based ceramic scintillator for x-ray imaging," Nucl. Instrum. Methods Phys. Res. A **488**, 579–590 (2002).

[79] V. V. Nagarkar *et al.*, "A new X-ray scintillator for digital radiography," IEEE Trans. Nucl. Sci. **50**, 297–300 (2003).